Available online at www.sciencedirect.com

ScienceDirect

Procedia Computer Science 00 (2022) 1–19

Procedia Computer Science

Implementation of micromorphic approaches to brittle fracture

David Siedel[a], Jacques Besson[b], Samuel Forest[b], Thomas Helfer[a], Olivier Fandeur[c,d]

[a]*CEA, DES/IRESNE/DEC/SESC/LSC, Département d'Études des Combustibles, Cadarache, France*
[b]*MINES ParisTech, PSL Research University, MAT - Centre des matériaux, CNRS UMR 7633, Evry BP 87 9103, France*
[c]*CEA, ISAS/DES/DM2S/SEMT/LM2S, Département de Modélisation des Systèmes et des Structures, Saclay, France*
[d]*IMSIA, UMR 8193, CNRS-EDF-CEA-ENSTA*
[e]*EDF R&D ERMES, 7 Boulevard Gaspard Monge, 91120 Palaiseau, France*

Abstract

This paper describes discusses a class of micromorphic damage behaviours for quasi-brittle materials in the variational framework of simple generalized standard materials. Their links with the classical AT1 and AT2 phase-field models is discussed. It is shown that those micromorphic damage behaviours can be seen as approximations of the latter. A numerical parameter allows to control the degree of approximation. Micromorphic damage behaviours exhibits the following advantages: (i) The irreversibility constraint is treated locally, at the integration points. (ii) The balance equations are standard partial derivative equations which can readily be solved by most FEM or FFT solvers. (iii) The variational framework allows the derivation of (at least) three alternate minimization schemes. Numerical experiments performed using `mgis.fenics` python module allow to compare numerically the presented micromorphic damage behaviours and the phase field AT1 and AT2 models on a set of tests classically used in the literature. Finally, those micromorphic damage behaviours have been implemented in the `mfem.mgis` library. This implementation is shown to perform well with higher order finite elements on a test proposed by *Alessi et al.* A description of the fragmentation of a nuclear fuel pellet demonstrates the applicability of those behaviours on large scale industrial problems.

© 2011 Published by Elsevier Ltd.

Keywords:
Computational mechanics, Brittle fracture

Contents

1. Introduction

The variational approach to brittle fracture takes its roots in the work of Francfort and Marigo [1, 2], which recasted the Griffith theory into an energy minimization problem. This revisted approach of the Griffith theory is however not tractable with standard numerical methods [3, 4], in particular the commonly used finite element method. For this reason, Bourdin *et al.* developed regularized versions [3] following the works of Ambrosio and Tortorelli [5].

Phase field approach to brittle fracture and damage irreversibility consition. The so-called phase-field approaches to fracture have since become widely popular. As pointed by Gerasimov and De Lorenzis in their excellent review [6], one of the main difficulties in the implementation of those approaches is the treatment of the irreversibility constraint (the damage can only increase), a question on which a considerable amount of works has been published (See *e.g.* [7, 8, 9, 10, 11, 12]). Most of the proposed solutions are not directly implemented in standard FEM or FFT solvers. An noticeable exception to this statement is the Miehe' alternative based an the so-called history variable [13]. However, Miehe' alternative is not variationally consistent.

Micromorphic approach to brittle fracture. A comprehensive framework for micromorphic approaches to various physical problems, including brittle fracture, has been developed by Forest in [14, 15]. Balance equations arising from such micromorphic approaches are standard partial differential equations, that can readily be solved by most FEM or FFT solvers. In particular, these micromorphic behaviours allow to deal with the damage irreversibility constraint at integration points, instead of having to deal with it in the resolution of balance equations, as is the case for the classical Phase field approach [6]. These advantages have been highlighted by Rezaee-Hajidehi *et al.* in the context of phase-field approaches to phase transformation [16]. Such micromorphic models were recently investigated by Bharali *et al.* [17] to approximate the AT1 and AT2 models using a monolithic resolution strategy.

Outline. Following Forest' micromorphic framework [14, 15], a class of micromorphic brittle behaviours that can approximate classical models of brittle fracture in a variationally consistent way is proposed in Section 2. The variational basis of the behaviour is exploited to derive three alternate minimization schemes in Section 4, whose convergence is guaranteed. Several test cases comparing the prediction of the classical AT2 model and its micromorphic counterpart are presented in Section 5, where the choice of the penalization parameter which at the foundation of the link between the Phase Field approach and the micromorphic one is discussed in-depth. Numerical experiments are presented in Section 5, which assess:

- The performance of the micromorphic approach with high order finite elements in the case of shear driven fracture.
- The scalability of the micromorphic approach.

2. The micromorphic approach to brittle fracture

2.1. Description of the coupled problem

Solid body in the current configuration. Let Ω_t a solid body that is subjected to a volumetric load $\boldsymbol{f}_v$ in the current configuration at some time $t > 0$. A displacement $\boldsymbol{u}_d$ is prescribed on the Dirichlet boundary $\partial_t\Omega_t$ and a surface load $\boldsymbol{t}_n$ is imposed on the Neumann boundary $\partial_n\Omega_t$.

Transformation mapping. Let $\boldsymbol{\Phi}$ the transformation mapping of the solid body from the initial configuration Ω to the current configuration Ω_t. The displacement field $\boldsymbol{u}$ is such that $\boldsymbol{u} = \boldsymbol{\Phi} - \boldsymbol{I}_d$ where $\boldsymbol{I}_d$ is the identity application on Ω. The gradient of the transformation is denoted $\underset{\sim}{\boldsymbol{F}} = \nabla\boldsymbol{\Phi} = \underset{\sim}{\boldsymbol{I}}_d + \nabla\boldsymbol{u}$. Let $\partial_D\Omega$ and $\partial_N\Omega$ the images of $\partial_t\Omega_t$ and $\partial_n\Omega_t$ respectively by $\boldsymbol{\Phi}^{-1}$.

External loads in the reference configuration. In the reference configuration, the solid is subjected to a volumetric load $\boldsymbol{f}_V$, a prescribed displacement $\boldsymbol{u}_D$ on $\partial_D\Omega$, and a surface load $\boldsymbol{t}_N$ on $\partial_N\Omega$, where the volumetric and surface loads $\boldsymbol{f}_V$ and $\boldsymbol{t}_N$ have been obtained from their counterparts $\boldsymbol{f}_v$ and $\boldsymbol{t}_n$ respectively, using Nanson formulaes. For the sake of simplicty, they are supposed to be independent on $\underset{\sim}{\boldsymbol{F}}$.

State of the solid. The mechanical state of the solid body Ω is characterized by the displacement field $\boldsymbol{u}$, the damage field d and a micromorphic damage field d_χ.

Free energy potential. The free energy potential ψ_Ω of the body Ω reads as a function of the displacement $\boldsymbol{u}$, the (local) damage d and the micromorphic damage d_χ, in the form

$$\psi_\Omega(\underset{\sim}{\boldsymbol{F}}, d, d_\chi, \nabla d_\chi) = \psi_{\underset{\sim}{\boldsymbol{F}},d}(\underset{\sim}{\boldsymbol{F}}, d) + \psi_d(d) + \psi_{d_\chi,d}(d_\chi, d) + \psi_{\nabla d_\chi}(\nabla d_\chi) \tag{1}$$

where $\psi_{\underset{\sim}{\boldsymbol{F}},d}$ denotes the mechanical contribution that takes into account the damage in the medium, ψ_d is the energy stored during the fracture process, ψ_{d,d_χ} is a coupling term between the damage and micromorphic damage variables, and $\psi_{\nabla d_\chi}$ defines the micromorphic force. In practice, ψ_Ω is a differentiable function.

Stresses. In the spirit of [14], the following stresses are introduced

$$\underset{\sim}{\boldsymbol{P}} = \frac{\partial\psi_\Omega}{\partial\underset{\sim}{\boldsymbol{F}}} \qquad \boldsymbol{b}_\chi = \frac{\partial\psi_\Omega}{\partial\nabla d_\chi} \qquad a_\chi = \frac{\partial\psi_\Omega}{\partial d_\chi} \qquad Y = -\frac{\partial\psi_\Omega}{\partial d} \tag{2}$$

where $\underset{\sim}{\boldsymbol{P}}$ is the first Piola-Kirchoff stress tensor, and $\boldsymbol{b}_\chi, a_\chi$ and Y are the thermodynamic forces associated to $\nabla d_\chi, d_\chi$ and d respectively.

Dissipation potential. A dissipation potential $\phi_\Omega(d)$ accounts for the irreversibility of the fracture process in the medium. For time independent mechanisms, ϕ_Ω is usually not differentiable. However, it is is assumed to be an homogeneous function of degree one such that for any time increment $\Delta t > 0$, and any admissible damage field d at the time $t + \Delta t$

$$\Delta t\,\phi_\Omega\left(\frac{d - d|_t}{\Delta t}\right) = \phi_\Omega(d - d|_t) \tag{3}$$

In particular, $\phi_\Omega(d)$ generally contains an indicator function to enforce the irreversibility of the damage evolution.

2.2. Lagrangian formulation of the coupled problem

Total Lagrangian. In the view of generalized standard materials [18, 19, 20, 21], and for any time increment $\Delta t > 0$, the equilibrium of the solid Ω at the time $t + \Delta t$ is characterized by the stationarity of the total incremental Lagrangian L_Ω^{tot} [22, 23] such that

$$L_\Omega^{\text{tot}} = \int_\Omega \psi_\Omega(\underset{\sim}{\boldsymbol{F}}, d, d_\chi, \nabla d_\chi) + \int_\Omega \Delta t\,\phi_\Omega\left(\frac{d - d|_t}{\Delta t}\right) - \int_\Omega \boldsymbol{f}_V \cdot \boldsymbol{u} - \int_{\partial_N\Omega} \boldsymbol{t}_N \cdot \boldsymbol{u}|_{\partial_N\Omega} \tag{4}$$

for any admissible displacement, damage and micromorphic damage fields $\boldsymbol{u}, d$ and d_χ at the time $t + \Delta t$. To satisfy the Ilyushin-Drucker postulate, the total incremental Lagrangian L_Ω^{tot} must be convex with respect to each variables $\boldsymbol{u}, d$ and d_χ taken independently. It can be shown that this condition is ensured if the free energy potential ψ_Ω and the dissipation potential ϕ_Ω are convex with respect to their respective arguments.

Total Lagrangian split. Deriving equilibrium equations from the principle of the minimum of the Lagrangian is non trivial due to the fact that the dissipation potential is not differentiable. It is then convenient to separate the total Lagrangian L_Ω^{tot} into two parts L_Ω^{hel} and L_Ω^{dis} as follows:

$$L_\Omega^{\text{hel}} = \int_\Omega \psi_\Omega(\underset{\sim}{\boldsymbol{F}}, d, d_\chi, \nabla d_\chi) - \int_\Omega \boldsymbol{f}_V \cdot \boldsymbol{u} - \int_{\partial_N\Omega} \boldsymbol{t}_N \cdot \boldsymbol{u}|_{\partial_N\Omega} \tag{5a}$$

$$L_\Omega^{\text{dis}} = \int_\Omega \phi_\Omega(d - d|_t) \tag{5b}$$

where (3) has been used in (5b).

2.3. The displacement and micromorphic damage problem

In this section, the condition on the regular part (5a) of the Lagrangian (4) is considered only. The evolution of the damage is discussed in Section 2.4.

Lagrangian variations. Following [24], the solid Ω is in equilibrium if the regular part of the Lagrangian L_Ω^{hel} is minimal with respect to the displacement field $\boldsymbol{u}$ and the micromorphic damage field d_χ. The first order variations of the Lagrangian (5a) with respect to $\boldsymbol{u}$ and d_χ respectively yields the weak equations

$$\langle \frac{\partial L_\Omega^{\text{hel}}}{\partial \boldsymbol{u}}, \delta\boldsymbol{u} \rangle = \int_\Omega \underset{\sim}{\boldsymbol{P}} : \nabla\delta\boldsymbol{u} - \int_\Omega \boldsymbol{f}_V \cdot \delta\boldsymbol{u} - \int_{\partial_N\Omega} \boldsymbol{t}_N \cdot \delta\boldsymbol{u}|_{\partial_N\Omega} \qquad \forall \delta\boldsymbol{u} \tag{6a}$$

$$\langle \frac{\partial L_\Omega^{\text{hel}}}{\partial d_\chi}, \delta d_\chi \rangle = \int_\Omega a_\chi\, \delta d_\chi + \int_\Omega \boldsymbol{b}_\chi \cdot \nabla d_\chi \qquad \forall \delta d^\chi \tag{6b}$$

Strong equation. Applying the divergence theorem, the following strong equations for the sole displacement problem are deduced from the weak equation (6a)

$$\nabla \cdot \underset{\sim}{\boldsymbol{P}} + \boldsymbol{f}_V = 0 \qquad \textit{balance of momentum} \tag{7a}$$

$$\underset{\sim}{\boldsymbol{P}} \cdot \boldsymbol{n} - \boldsymbol{t}_N = 0 \qquad \textit{continuity of the normal stress} \tag{7b}$$

Similarly, the strong equations governing the sole micromorphic damage problem are deduced from (6b)

$$\nabla \cdot \boldsymbol{b}_\chi - a_\chi = 0 \qquad \textit{balance of micromorphic damage momentum} \tag{8a}$$

$$\boldsymbol{b}_\chi \cdot \boldsymbol{n} = 0 \qquad \textit{micromorphic damage boundary conditions} \tag{8b}$$

where the governing laws of the micromorphic damage variable define a generalized continuum medium as introduced in [14].

2.3.1. Evolution of the displacement

Mechanical potential. $\psi_{\underset{\sim}{\boldsymbol{F}},d}$ determines the expression of the stress and contributes to the thermodynamic force driving the damage evolution. A classical choice consists in multiplying the free energy of an undamaged material $\psi_{\underset{\sim}{\boldsymbol{F}}}$ by a degradation function $g(d)$ such that

$$\psi_{\underset{\sim}{\boldsymbol{F}},d}(\underset{\sim}{\boldsymbol{F}}, d) = g(d)\, \psi_{\underset{\sim}{\boldsymbol{F}}}(\underset{\sim}{\boldsymbol{F}}) \tag{9a}$$

$$\underset{\sim}{\boldsymbol{P}} = g(d)\, \frac{\partial \psi_{\underset{\sim}{\boldsymbol{F}}}}{\partial \underset{\sim}{\boldsymbol{F}}} \tag{9b}$$

Mechanical potential deviatoric split. In order to account for the possible dependance of the damage driving force on the stress state, a decomposition [25, 13] of the mechanical free energy density $\psi_{\underset{\sim}{\boldsymbol{F}}}$ into a deviatoric part $\psi_{\underset{\sim}{\boldsymbol{F}}\text{dev}}$ and into a spherical part $\psi_{\underset{\sim}{\boldsymbol{F}}\text{sph}}$ is commonly assumed. The degradation function $g(d)$ then acts on either one the two components $\psi_{\underset{\sim}{\boldsymbol{F}}\text{dev}}$ or $\psi_{\underset{\sim}{\boldsymbol{F}}\text{sph}}$ hence defining either *shear driven fracture* or *pressure driven fracture*

Mechanical potential spectral split. Another classical choice proposed by Miehe [13] consists in using a spectral decomposition of the strain to split the free energy into a positive $\psi_{\underset{\sim}{\boldsymbol{F}}+}$ and a negative $\psi_{\underset{\sim}{\boldsymbol{F}}-}$ part. In this case, the degradation function is only applied to the positive part $\psi_{\underset{\sim}{\boldsymbol{F}}+}$ of the free energy, in order to account for *traction driven fracture* processes.

Micromorphic damage coupling potential. The free energy density $\psi_{d_\chi,d}$ is chosen such that it penalizes the difference between the damage field d and the micromorphic damage field d_χ such that

$$\psi_{d_\chi,d}(d_\chi, d) = \frac{H_\chi}{2}\left(d - d_\chi\right)^2 \tag{10a}$$

$$a_\chi = -H_\chi\left(d - d_\chi\right) \tag{10b}$$

2.3.2. Evolution of the micromorphic damage

Micromorphic damage gradient potential. The free energy density $\psi_{\nabla d_\chi}$ is chosen such that it penalizes the localization of the micromorphic damage field d_χ and

$$\psi_{\nabla d_\chi}(\nabla d_\chi) = \frac{A_\chi}{2}\,\nabla d_\chi \cdot \nabla d_\chi \tag{11a}$$

$$\boldsymbol{b}_\chi = A_\chi\,\nabla d_\chi \tag{11b}$$

Damage and micromorphic damage relation. Substituting (10b) and (11b) in the expression of the governing equation (8a) shows that the micromorphic damage d_χ satisfies the Laplace equation [14]

$$A_\chi\,\nabla^2 d_\chi + H_\chi\left(d - d_\chi\right) = 0 \tag{12}$$

where ∇^2 denotes the Laplacian operator.

2.4. The damage problem

Damage driving force. Following the definition of mechanical and micromorphic damage related potentials given in Section 2.3, the expression of the thermodynamic force Y associated with the damage field is given by:

$$\begin{aligned} Y &= -\frac{dg}{dd}\,\psi_{\underset{\sim}{\boldsymbol{F}}}(\underset{\sim}{\boldsymbol{F}}) - \frac{d\psi_d}{dd} - \frac{\partial \psi_{d_\chi,d}}{\partial d} \\ &= -\frac{dg}{dd}\,\psi_{\underset{\sim}{\boldsymbol{F}}}(\underset{\sim}{\boldsymbol{F}}) - \frac{d\psi_d}{dd} + a_\chi \end{aligned} \tag{13}$$

where (10a) has been used.

Dissipative part of the Lagrangian. Following [24, 18, 19], at each point the thermodynamic force Y associated with the damage is assumed to be in the subgradient of the dissipation potential:

$$Y \in \partial\phi_\Omega \tag{14}$$

Dissipation potential. A simple choice for the dissipation potential is

$$\phi_\Omega(\dot{d}) = Y_0\,\dot{d} + \mathrm{I}_{\mathbb{R}_+}(\dot{d}) \tag{15}$$

where Y_0 is a scalar threshold value, and $\mathrm{I}_{\mathbb{R}_+}$ denotes the characteristic function associated with positive real number such that

$$\mathrm{I}_{\mathbb{R}_+}(x) = \begin{cases} 0 & \text{if} \quad x \geq 0 \\ +\infty & \text{if} \quad x < 0 \end{cases} \tag{16}$$

Yield surface. The dissipation potential (15) is equivalent to define the damage surface

$$Y = Y_0 \tag{17}$$

leading to an evolution of the damage driven by the following Karush–Kuhn–Tucker conditions

$$\Delta d\,(Y - Y_0) = 0 \tag{18a}$$
$$\Delta d \geq 0 \tag{18b}$$
$$Y - Y_0 \leq 0 \tag{18c}$$

Combining equations (12), (13) and (17), the yield surface may also be written:

$$\frac{dg}{dd}\,\psi_{\underset{\sim}{\boldsymbol{F}}}(\underset{\sim}{\boldsymbol{F}}) = Y_0 + \frac{d\psi_d}{dd} - H_\chi(d - d_\chi) \tag{19}$$

which yields that d is an implicit function of d_χ

3. Link with classical models of brittle fracture

Total resulting Lagrangian. Choices described by equations (9), (15) and (11a) lead to the following expression of the total Lagrangian (4)

$$\begin{aligned} L_\Omega^{\text{tot}} = &\int_\Omega g(d)\,\psi_{\underset{\sim}{\boldsymbol{F}}}(\underset{\sim}{\boldsymbol{F}}) + \int_\Omega \psi_d(d) + \int_\Omega Y_0\,d + \int_\Omega \frac{A_\chi}{2}\,\nabla d_\chi \cdot \nabla d_\chi \\ &+ \int_\Omega \frac{H_\chi}{2}\left(d - d_\chi\right)^2 + \int_\Omega \mathrm{I}_{\mathbb{R}_+}(d - d|_t) \\ &- \int_\Omega \boldsymbol{f}_V \cdot \boldsymbol{u} - \int_{\partial_N\Omega} \boldsymbol{t}_N \cdot \boldsymbol{u}|_{\partial_N\Omega} \end{aligned} \tag{20}$$

where the constant term $Y_0\,d|_t$, which thus does not have any influence of the solution, has been removed from the expression of the Lagrangian.

Equal damage and micromorphic field limit case. For high values of H_χ, the contribution to the potential $\psi_{d_\chi,d}$ may be seen as a penalization term which ensures that the damage d and the micromorphic damage d_χ are equal in a weak sense. Intuitively, if $H_\chi \to \infty$, these two must become equal to ensure a finite energy. The Lagrangian (20) is thus expected to have the following limit

$$\begin{aligned} L_\Omega^{\text{tot}} = &\int_\Omega g(d)\,\psi_{\underset{\sim}{\boldsymbol{F}}}(\underset{\sim}{\boldsymbol{F}}) + \int_\Omega \psi_d(d) + \int_\Omega Y_0\,d + \int_\Omega \frac{A_\chi}{2}\,\nabla d \cdot \nabla d \\ &+ \int_\Omega \mathrm{I}_{\mathbb{R}_+}(d - d|_t) \\ &- \int_\Omega \boldsymbol{f}_V \cdot \boldsymbol{u} - \int_{\partial_N\Omega} \boldsymbol{t}_N \cdot \boldsymbol{u}|_{\partial_N\Omega} \end{aligned} \tag{21}$$

and Lagrangian (21) can be identified with Lagrangians describing many classical models of brittle fracture with appropriate choices of $g(d)$, ψ_d, A_χ and Y_0.

3.1. Link with Ambrosio–Tortorelli regularization models

Ambrosio–Tortorelli [5] regularization of the initial variational approach to fracture [1], originally introduced in [3], have become widely used in the computational mechanics community. Several works have shown that the regularized solution converges in the sense of the so-called Γ- convergence, to the solution of the initial problem in some specific cases (See *e.g.* [3]).

Values of the AT1 model. Two regularization models were introduced in [5]. The first one, namely the AT1 model, allows to recover the initial problem formulated in [1] for infinitely small values of the characteristic length defining the thckness of the smeared crack, and such that initiation of damage occurs on the onset of some yield criterion. Choosing the following potentials and values for the definition of the micromorphic model allows to recover the AT1 model

$$g(d) = (1 - d) \tag{22a}$$

$$\psi_d(d) = \frac{3\,G_c}{8\,\ell_c}\,d \tag{22b}$$

$$A_\chi = \frac{3}{4}\,G_c\,\ell_c \tag{22c}$$

$$Y_0 = 0 \tag{22d}$$

where G_c is a fracture energy, and ℓ_c is the characteristic length.

Values of the AT2 model. The second regularization model in [5] introduces a quadratic fracture energy potential, such that damage occurs on the onset of deformation of the medium. Choosing the following potentials and values for the definition of the micromorphic model allows to recover the AT2 model

$$g(d) = (1 - d)^2 \tag{23a}$$

$$\psi_d(d) = \frac{G_c}{2\,\ell_c}\,d \tag{23b}$$

$$A_\chi = G_c\,\ell_c \tag{23c}$$

$$Y_0 = 0 \tag{23d}$$

3.2. Link with Lorentz model

Values of Lorentz model. AT1 and AT2 regularization models proposed by [26] introduce the characteristic length ℓ_c, that controls the thickness of the smeared crack. As stated in [27, 28], this regularization length defines the yield strength of the medium. In numerical applications, the strength of the material is thus mesh dependant, since the value of characteristic length must be greater than the element size in order to be captured. Therefore, Lorentz *et. al.* [29, 30] alleviated this constraint by proposing an extension of the regularization proposed in [26], that introduces a state variable γ related to the yield strength of the material. The following values for the proposed micromorphic approach hence yield Lorentz gradient damage model

$$g(d) = \left(\frac{1 - d}{1 + \gamma\,d}\right)^2 \tag{24a}$$

$$\psi_d(d) = \frac{3\,G_c}{8\,\ell_c}\,d \tag{24b}$$

$$A_\chi = \frac{3}{4}\,G_c\,\ell_c \tag{24c}$$

$$Y_0 = 0 \tag{24d}$$

where γ is the aforementioned parameter of the Lorentz' model.

Alternative choices regarding the role of the fracture energy. Note that an alternative choice can be made for both AT1 and Lorentz' models such that

$$\psi_d(d) = 0 \quad \text{and} \quad Y_0 = \frac{3}{8}\,G_c\,\ell_c \tag{25}$$

While leading the same Lagrangian, this alternative choice has a totally different physical meaning, since part of the fracture energy is now considered as dissipated rather than stored. Since neither crack healing nor coupling with heat transfer are considered, those choices are equivalent in the context of this paper.

4. Resolution schemes

4.1. A first alternate minimization scheme

Alternate scheme. Observing that the Lagrangian (20) is not convex *globally*, but convex with respect to each variable taken independently, an alternate minimization scheme is the spirit of that proposed by Bourdin *et al.* in [3] is devised. It consists in the following iterative scheme

$$\begin{cases} \boldsymbol{u}^{(n+1)} = \underset{\hat{\boldsymbol{u}}}{\operatorname{argmin}}\, L_\Omega^{\mathrm{tot}}(\hat{\boldsymbol{u}}, d^{(n)}, d_\chi^{(n)}) \\ d_\chi^{(n+1)} = \underset{\hat{d}_\chi}{\operatorname{argmin}}\, L_\Omega^{\mathrm{tot}}(\boldsymbol{u}^{(n+1)}, d^{(n)}, \hat{d}_\chi,) \\ d^{(n+1)} = \underset{\hat{d}}{\operatorname{argmin}}\, L_\Omega^{\mathrm{tot}}(\boldsymbol{u}^{(n+1)}, \hat{d}, d_\chi^{(n+1)},) \end{cases} \tag{26}$$

where $\boldsymbol{u}^{(n)}$, $d^{(n)}$ and $d_\chi^{(n)}$ denote respectively the estimates of the displacement field, micromorphic damage field and damage field at the n$^{\text{th}}$ iteration of the algorithm. In particular, each step of the algorithm diminishes the value of the Lagrangian, ensuring the convergence of the scheme. Minimization with respect to $\boldsymbol{u}$ and d_χ leads to solving the two standard Partial Differential Equations (PDE) (7a) and (8a).

Displacement problem. Considering a linear thermo-elastic material for the definition of the potential $\psi_{\underset{\sim}{\boldsymbol{F}}}$, the PDE associated with $\boldsymbol{u}$ is a linear elastic problem with spatially variable mechanical coefficients. This problem becomes non linear if unilateral effects are taken into account.

Micromorphic damage problem. The PDE associated with d_χ is always linear and $d_\chi^{(n+1)}$ is the solution of (see Equation (12))

$$-A_\chi\, \nabla^2\, d_\chi^{(n+1)} + H_\chi\, d_\chi^{(n+1)} = H_\chi\, d^{(n)} \tag{27}$$

Note that this PDE is close to the PDE describing heat transfer and can thus be solved in most finite element solvers. See [31] for an alternative implementation of the phase-field model based on this analogy.

Damage problem. Minimization with respect to the damage d is local and depends on the considered model.

4.2. A second alternate minimization scheme

Since an update of the damage variable is computationally inexpensive, compared to the computation of the displacement and micromorphic damage, one may consider evaluating its value twice, as follows:

$$\begin{cases} \boldsymbol{u}^{(n+1)} = \underset{\hat{\boldsymbol{u}}}{\operatorname{argmin}}\, L_\Omega^{\mathrm{tot}}(\hat{\boldsymbol{u}}, d^{(n)}, d_\chi^{(n)}) \\ d^{(n+1/2)} = \underset{\hat{d}}{\operatorname{argmin}}\, L_\Omega^{\mathrm{tot}}(\boldsymbol{u}^{(n+1)}, \hat{d}, d_\chi^{(n)},) \\ d_\chi^{(n+1)} = \underset{\hat{d}_\chi}{\operatorname{argmin}}\, L_\Omega^{\mathrm{tot}}(\boldsymbol{u}^{(n+1)}, d^{(n+1/2)}, \hat{d}_\chi,) \\ d^{(n+1)} = \underset{\hat{d}}{\operatorname{argmin}}\, L_\Omega^{\mathrm{tot}}(\boldsymbol{u}^{(n+1)}, \hat{d}, d_\chi^{(n+1)},) \end{cases} \tag{28}$$

where the damage estimate $d^{(n+1/2)}$ is given by an appropriate modification of Equation (19).

4.3. A third alternate minimization scheme

The third alternate minimization scheme is based on the fact that the minimization with respect to d and d_χ is convex

Dependant variables. Since the micromorphic damage field d_χ is an implicit functions of the damage field d (See Equation (19)), the total derivative of the micromorphic thermodynamic force a_χ is given by

$$\frac{da_\chi}{dd_\chi} = \frac{\partial a_\chi}{\partial d_\chi} + \frac{\partial a_\chi}{\partial d}\frac{\partial d}{\partial d_\chi} \tag{29}$$

where the expression of the derivative of the damage field with respect to the micromorphic damage field $\partial d/\partial d_\chi$ is deduced from (19). As $\partial d/\partial d_\chi$ is only linear by part, Equation (8a) is indeed non-linear.

Non-linear micromorphic damage and displacement resolution scheme. Consequently, the following iterative scheme is considered where the evolution of d_χ is still given by Equation (8a) but the where the determination of the conjugated force a_χ is given by Equation (29).

$$\begin{cases} \boldsymbol{u}^{(n+1)} = \underset{\hat{\boldsymbol{u}}}{\operatorname{argmin}}\, L_\Omega^{\text{tot}}(\hat{\boldsymbol{u}}, d^{(n)}, d_\chi^{(n)}) \\ d_\chi^{(n+1)}, d^{(n+1)} = \underset{\hat{d}_\chi, \hat{d}}{\operatorname{argmin}}\, L_\Omega^{\text{tot}}(\boldsymbol{u}^{(n+1)}, \hat{d}, \hat{d}_\chi,) \end{cases} \tag{30}$$

5. Numerical implementations using standard finite elements

In this section, the proposed micromorphic apporoach to brittle fracture is evaluated on numerical applications. The first three are classical test cases taken from the literature and have been performed using the `mgis.fenics` implementation. Implementations are freely available on the following repository: `https://github.com/davidsiedel/h2o_paper`. They aim at comparing both the classical phase field approach to the proposed micromorphic one. The last two test cases are performed using the `mfem.fenics` implementation, and showcase respectively the performance of the micromorphic approach with high order finite elements in the case of shear driven fracture, and the scalability of the approach.

Hypotheses. For the first two and the last applications in this section, a spectral decomposition of the thermo-elastic energy potential $\psi_{\underset{\sim}{\boldsymbol{\varepsilon}}}$ in the framework of small deformations is considered, where $\underset{\sim}{\boldsymbol{\varepsilon}}$ denotes the linearized strain tensor. Test cases in 2 dimension assume a plane strain hypothesis. The penalization parameter H_χ is chosen as

$$H_\chi = \beta \frac{G_c}{\ell_c} \tag{31}$$

where β is a normalized penalization parameter [17].

Choice of the convergence criterion of the staggered schemes. In this paper, the staggered schemes are stopped when the damage becomes stationnary, i.e. when the absolute difference between two estimates of the damge is below a given threshold ε_d at each integration point. This criterion is not totally satisfying as it does not ensure that a true minimum of the Lagrangian is found. Therefore, this second criterion has been carefully checked for each steps of the numerical experiments described in this section.

5.1. Tensile test on a fiber reinforced matrix

Specimen and loading. The considered test case taken from [3] describes a matrix represented by a square of length 1mm, that is attached to a fiber in the middle (see Figure 1). The fiber is depicted by a hole of radius 0.2mm located at the center of the specimen, and is considered to be infinitely stiff with respect to the matrix. A vertical displacement of amplitude 0.125mm is applied at the top of the specimen, and the matrix is clamped around the fiber in both directions. Damage is enforced to be null at the intersection between the matrix and the fiber, and natural boundary conditions are considered elsewhere.

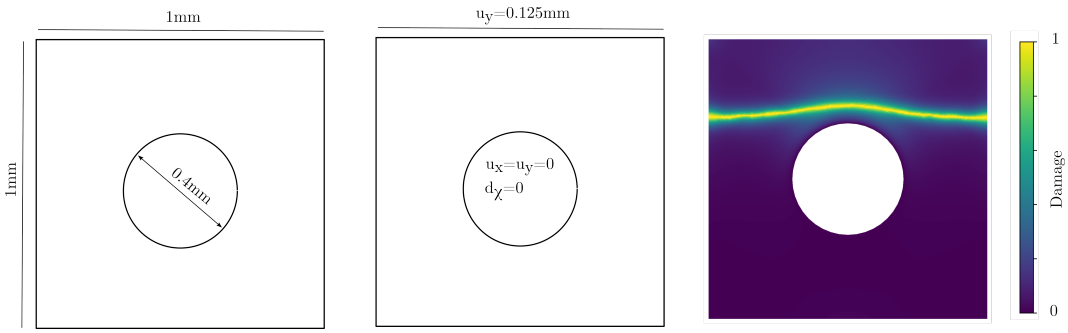

Figure 1. Geometry, boundary conditions and damage pattern

Material behaviour. A linear thermo-elastic energy potential $\psi_{\underset{\sim}{\varepsilon}}$ is considered, with a Young's modulus E equal to 200 MPa. The material displays a compressible behaviour with a Poisson's ratio ν equal to 0.2. The chosen micromorphic model is that corresponding to a AT2 model, and is described by Equations (23), where the fracture energy release rate G_c is equal to 1 J/mm^2, and the characteristic length is ℓ_c = 0.02 mm. Moreover, the degradation function acts on the spherical part of free energy potential (See Section 2.3.1)

Force delfection curve. Figure 2 displays the force-deflection curves for the tensile test on a fiber reinforced matrix, using either the proposed micromorphic approach, an AT2 phase field approach based on the resolution of the Karush–Kuhn–Tucker conditions to enforce irreversibility of the damage field, or an AT2 phase field approach based on the definition of Miehe's history function [13]. The third resolution scheme depicted in Section 4.3 is considered for the micromorphic approach. As illustrated by Figure 2, the force-displacement curve of the third scheme is very similar to the standard AT2 model based on the resolution of the variational inequality.

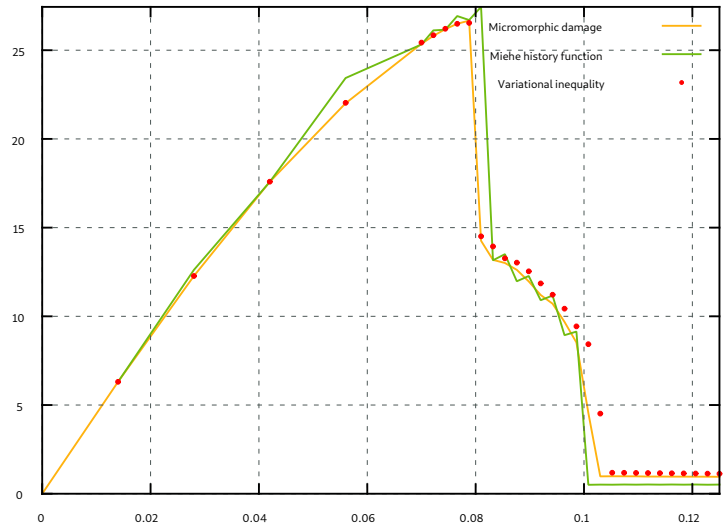

Figure 2. Evolution of the force as a function of the imposed displacement for the fiber reinforced matrix test for the third scheme with β = 150 and the standard phase-field schemes based on the resolution of the variational inegality or based on Miehe' history function [13]

5.2. Shear test on a notched plate

Specimen and loading. The second test case describes a square plate of length 1mm, that is clamped at the bottom in the vertical direction (see Figure 3). A tangential displacement of amplitude 0.125mm is applied at the top of the specimen, and one of the vertices of the plate is fixed to prevent rigid body motions in the tangential direction.

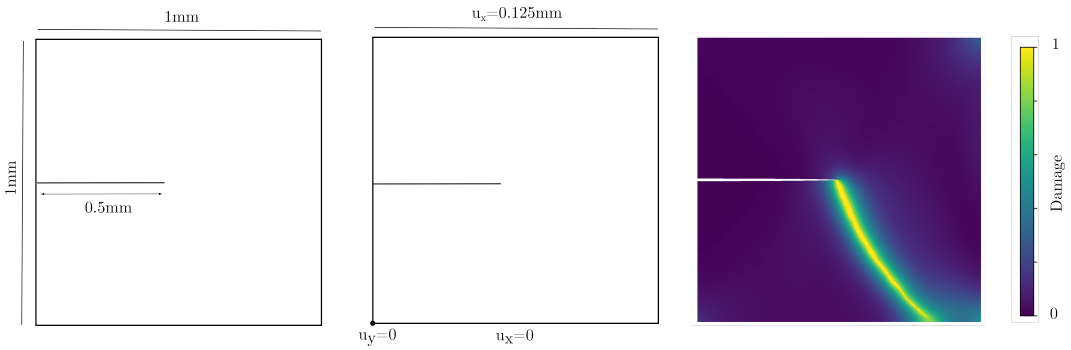

Figure 3. Geometry, boundary conditions and damage pattern

Material behaviour. As for the precedent test case, a linear elastic energy potential $\psi_{\underline{\underline{\varepsilon}}}$ is considered, with a Young's modulus $E = 200$ MPa and a Poisson's ratio $\nu = 0.2$. The chosen micromorphic damage is also described by Equations (23), with a fracture energy release rate $G_c = 1$ J/mm^2, and a characteristic length $\ell_c = 0.02$ mm. The degradation function acts on the spherical part of free energy potential (See Section 2.3.1)

Force delfection curve. Figure 4 displays the force-deflection curve of the shear test, for the proposed micromorphic approach based on the third resolution scheme described in Section 4.3 for several values of the penalization parameter β. As illustrated by Figure 4, the penalization factor plays a major role on the overall force-deflection curve. Experiments show that a value of $\beta = 150$ leads to undistinguishable results with those obtains using the AT2 model based on the resolution of the variational inequality to enforce damage irreversibility.

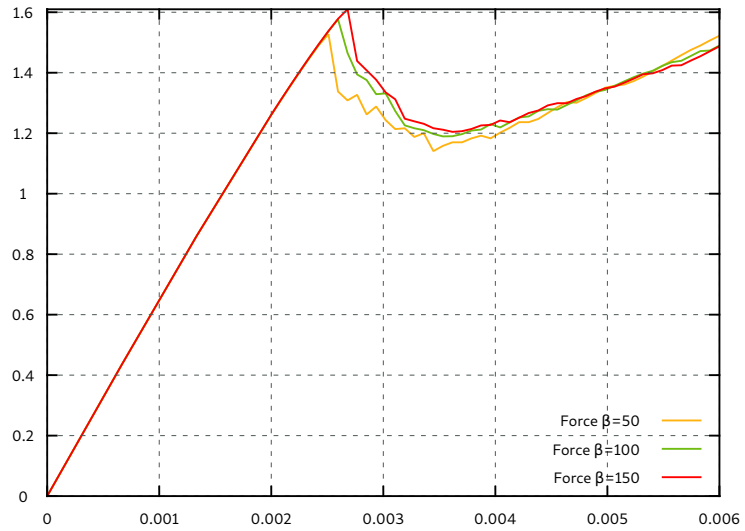

Figure 4. Evolution of the force as a function of the imposed displacement for $\beta = 50$, $\beta = 100$, $\beta = 150$ for the shear test using the third staggered scheme

Number of iterations. Figure 5 gives the number of iterations needed to achieve convergence of the fixed point algorithm for the shear test, using the proposed micromorphic approach based on the third resolution scheme, and for the AT2 phase field approach based on the resolution of the Karush–Kuhn–Tucker conditions to enforce irreversibility of the damage field. The number of iteration is roughly similar between the standard AT2 model and the third scheme, although a bit higher in general, as depicted on Figure 5.

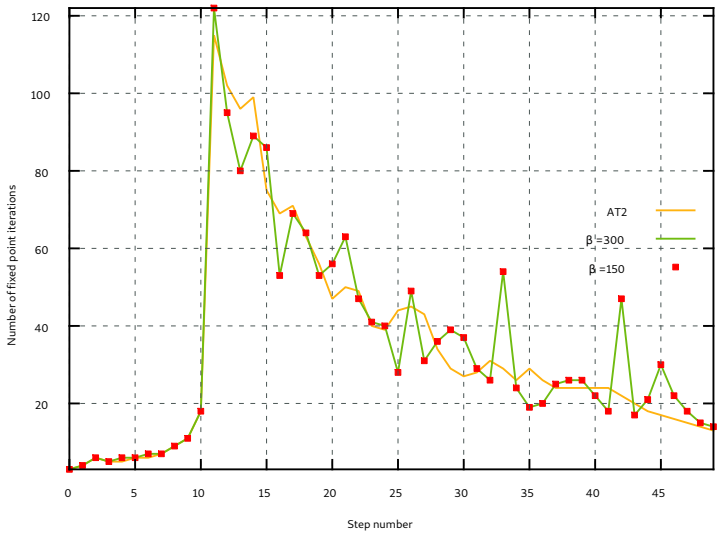

Figure 5. Number of iterations of the fixed point algorithm for the shear test as a function of the step number for the standard AT2 model and the third scheme for $\beta = 150$ and $\beta = 300$

Fracture energy. Figure 6 gives the evolution of the fracture energy as a function of the imposed displacement, for the proposed micromorphic approach and the third resolution scheme. Values are compared to those obtained with the standard AT2 phase field model based the variational resolution of the evolution of damage. A value of $\beta = 300$ is needed here to recover the energy dissipated by fracture for the AT2 model.

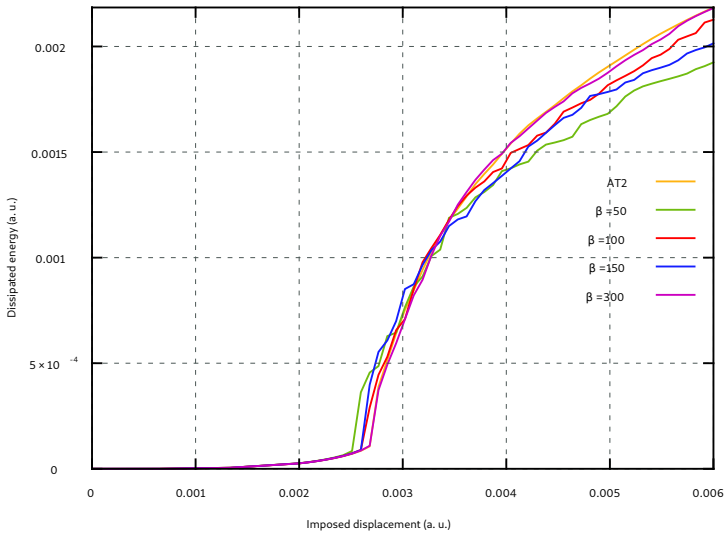

Figure 6. Evolution of the fracture energy as a function of the imposed displacement for $\beta = 50$, $\beta = 100$, $\beta = 150$ for the shear test using the third staggered scheme

5.3. Shear driven fracture on a tensile test

Spaciemn and loading. The considered test case taken from [32] describes a simple rectangular rod of length 2mm and width 1mm. A vertical displacement of amplitude 0.125mm is applied at the top of the specimen, and the bottom

is clamped in the vertical direction. One of the vertices of the plate is fixed in the tangential direction to prevent rigid body motions. Natural boundary conditions are considered elsewhere.

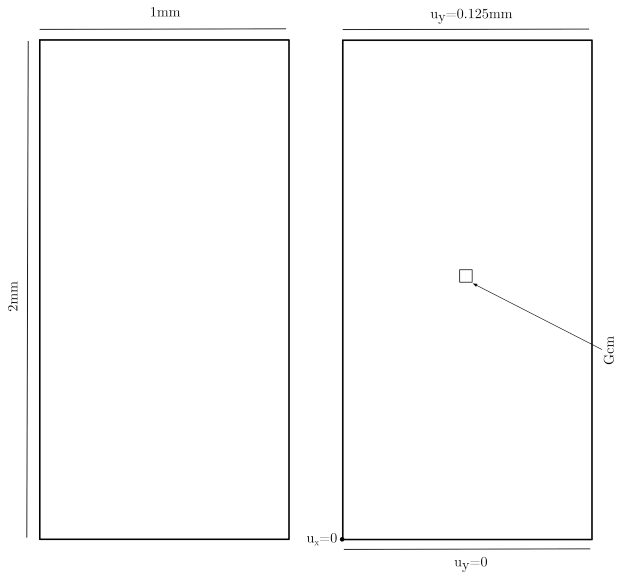

Figure 7. Geometry, boundary conditions and defect zone for the shear driven fracture test case

Material behaviour. *Alessi et al.* proposed a model to describe deviatoric driven fracture using the following choice of the elastic free energy $\psi_{\underset{\sim}{\boldsymbol{\varepsilon}},d}$

$$\psi_{\underset{\sim}{\boldsymbol{\varepsilon}},d}(\underset{\sim}{\boldsymbol{\varepsilon}}, d) = \frac{\mu}{2}\, g(d)\, \underset{\sim}{\boldsymbol{\varepsilon}}^{\mathrm{dev}} : \underset{\sim}{\boldsymbol{\varepsilon}}^{\mathrm{dev}} + \frac{K}{2}\, \underset{\sim}{\boldsymbol{\varepsilon}}^{\mathrm{sph}} : \underset{\sim}{\boldsymbol{\varepsilon}}^{\mathrm{sph}} \tag{32}$$

where $K = 175$ GPa is the bulk modulus, $\mu = 80.77$ Gpa is the shear modulus, $\underset{\sim}{\boldsymbol{\varepsilon}}^{\mathrm{dev}}$ is the deviatoric part of the elastic strain, and $\underset{\sim}{\boldsymbol{\varepsilon}}^{\mathrm{sph}}$ is the spherical part. The chosen micromorphic damage is described by Equations (23), with a fracture energy release rate $G_c = 2.7$ J/mm^2, and a characteristic length $\ell_c = 0.025$ mm. For damage initiation to localize at the center of the specimen, a degraded fracture energy release rate $G_c^m = 0.99 G_c$ is imposed in a square of size 0.05mm at the middle of the rod.

Quasi-incompressible behaviour. As stated by *Alessi et al.*, this model leads to quasi-incompressible behaviour in highly damaged zones, and Lagrange elements are not able to properly describe the damage localization band as well as the energy dissipated by the crack propagation. They then showed that various classical approaches (selective reduced integration and mixed displacement/pressure formulation) can overcome this issue. This test case is adapted to demonstrate that the micromorphic approach can be used with higher order finite elements in order to alleviate this issue. In the following, the same order of approximation are used to solve both the mechanical and the micromorphic problems.

Mesh description. The rod is discretized with triangle elements. The number of elements used as a function of the finite element order is given in Table 1. In practice, the number of elements have little influence on the results and the conclusions drawn in the next paragraph. A very fine mesh is used for low order finite elements (1 and 2) with several dozen elements inside the damage band (See Figure 8). A coarser mesh is used for higher order elements (4 and 6) with 4 to 6 elements inside the damage band.

Resolution Method	Memory footprint
Order 1	102 272 elements
Order 2	409 088 elements
Order 4	25 568 elements
Order 6	25 568 elements

Table 1. Geometry and material parameters for the shear driven fracture test

Damage pattern for low order elements. Figure 8 describes the damage pattern after the propagation of the crack. As described by *Alessi et al.*, volumetric locking leads to a spurious damage localization band with excessive thickness, *i.e.* a thickness largely greater than the characteristic length ℓ_c. A very fine mesh is used to demonstrate that the issue is not solved by mesh refinement.

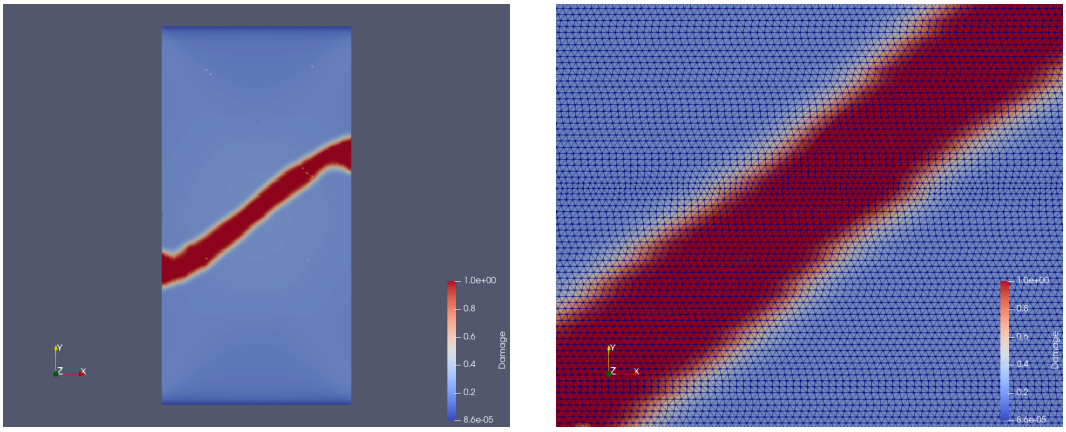

Figure 8. Spurious damage map obtained with linear elements (left). Zoom on the shear fracture (right)

Damage pattern for high order elements. Figure 9 show the results obtained with higher order elements. While the simulation with quadratic elements still exhibit a spurious damage localisation band, similar to the one observed with linear elements in Figure 8, higher order elements lead to satisfying results, i.e. higher order elements alleviate issues related to volumetric locking.

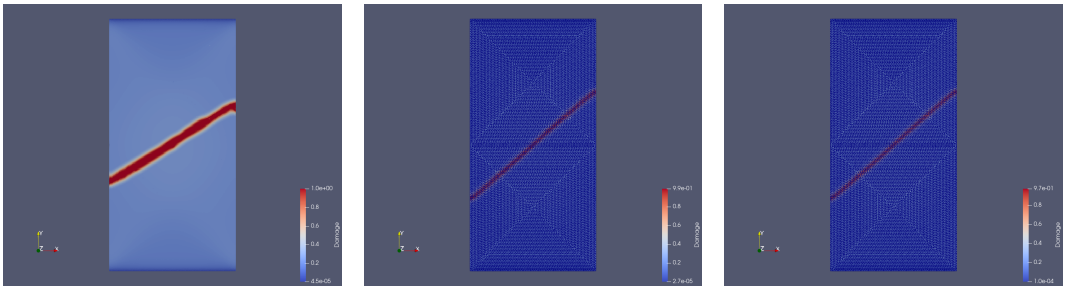

Figure 9. Damage map for higher order elements. Quadradic elements (left), fourth order elements (center), sixth order elements (right). The quadratic mesh is too fine to be shown without hiding the results

Force deflection curves. Figure 10 presents the force/displacement curves as a function of the finite element order. Quadratic results, which are intermediate between linear and quadratic results, are not reproduced for the sake of clarity.

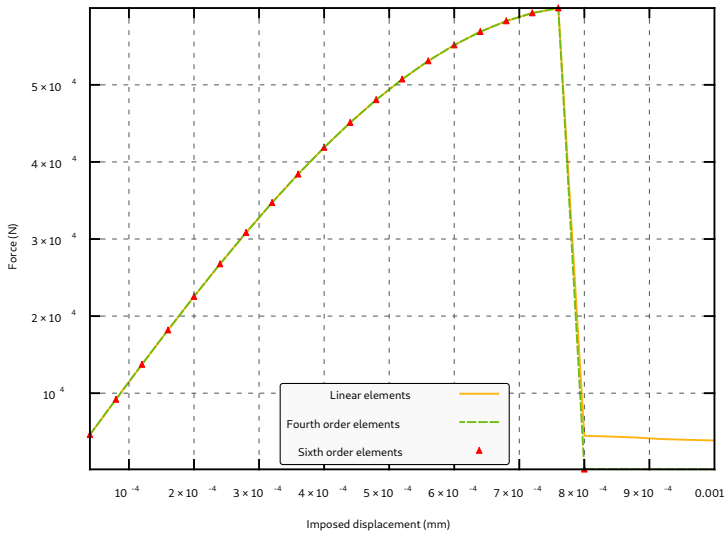

Figure 10. Traction curve

Observations. All order of approximations give similar results up to the crack propagation. The traction curve given by linear elements exhibits a residual stiffness and a spurious dissipation after the crack propagation. Fourth order and sixth order give undistinguishable results. In both cases, the force drops to zero after the crack propagation.

5.4. Fragmentation of a nuclear fuel pellet

Spaciemn and loading. This test case describes the fragmentation of a nuclear fuel pellet during the reactor start-up. The pellet is a cylinder of width 8.17mm and height 13.4mm. The top and bottom surfaces are recessed by a dishing of diameter 6.1mm and height 0.32mm. The pellet is fixed at one point to prevent rigid body motions. Assuming a constant thermal conductivity, a temperature load $T(r,t)$ is imposed in the pellet such that

$$T(r,t) = (T_{\mathrm{c}} - T_{\mathrm{o}})t\,(1 - r^2) + T_{\mathrm{o}} \tag{33}$$

where $T_c = 1500$K is the core temperature, $T_o = 600$K is the outer surface temperature, and r is the radial component such that $r = 0$ on the symmetry axis of the pellet, and t is a pseudo-time loading parameter in the range $[0, 1]$.

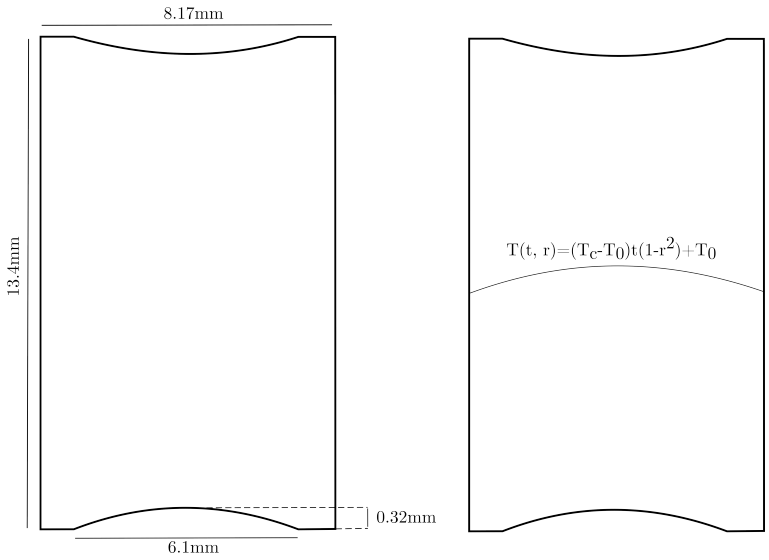

Figure 11. Geometry, boundary conditions and defect zone for the pellet

Material behaviour. A linear thermo-elastic free energy potential is considered, such that

$$\psi_{\underset{\sim}{\boldsymbol{\varepsilon}},d}(\underset{\sim}{\boldsymbol{\varepsilon}}, d, T) = g(d)\,\psi^{\text{th}}_{\underset{\sim}{\boldsymbol{\varepsilon}}}(\underset{\sim}{\boldsymbol{\varepsilon}}, T) \tag{34}$$

where the thermo-elastic potential $\psi^{\text{th}}_{\underset{\sim}{\boldsymbol{\varepsilon}}}$ is such that

$$\psi^{\text{th}}_{\underset{\sim}{\boldsymbol{\varepsilon}}}(\underset{\sim}{\boldsymbol{\varepsilon}}, T) = (\underset{\sim}{\boldsymbol{\varepsilon}} - \alpha\,(T - T_{\text{ref}})\,\underset{\sim}{\boldsymbol{I}}) : \underset{\approx}{\boldsymbol{C}} : (\underset{\sim}{\boldsymbol{\varepsilon}} - \alpha\,(T - T_{\text{ref}})\,\underset{\sim}{\boldsymbol{I}}) \tag{35}$$

with $\underset{\approx}{\boldsymbol{C}}$ the Hooke tensor defined by the Young modulus $E = 150$GPa and the Poisson ratio $\nu = 0.3$, the thermal expansion reference temperature $T_{\text{ref}} = 273$K and the linear mean thermal expansion coefficient $\alpha = 1 \cdot 10^{-5}\text{K}^{-1}$. The chosen micromorphic damage is described by Equations (23), with a fracture energy release rate $G_c = 2.7$ J/mm^2, and a characteristic length $\ell_c = 0.025$ mm. For damage initiation to localize anywhere in the specimen, a random uniform distribution of the fracture energy release rate with a mean value $G_c^{\text{mean}} = G_c$ and a standard deviation $G_c^{\text{std}} = XXX$ is imposed in the pellet.

Large scale computation. Damage patterns for the cracking of the fuel pellet are given in Figure 12. The mesh is composed of 33 230 848 triangles and 132 923 392 nodes, leading to a mechanical problem with 22.10^6 degrees of freedom. This large scale test case assesses the adaptivity of the micromorphic approach to industrial applications. Using the micromorphic approach, the irreversibility condition for the damage field is dealt with at quadrature points, and is thus fully parallel, hence avoiding the need to deploy the 132 923 392 Lagrange multipliers that would have been necessary for the AT2 model based on the variational treatment of the irreversibility condition.

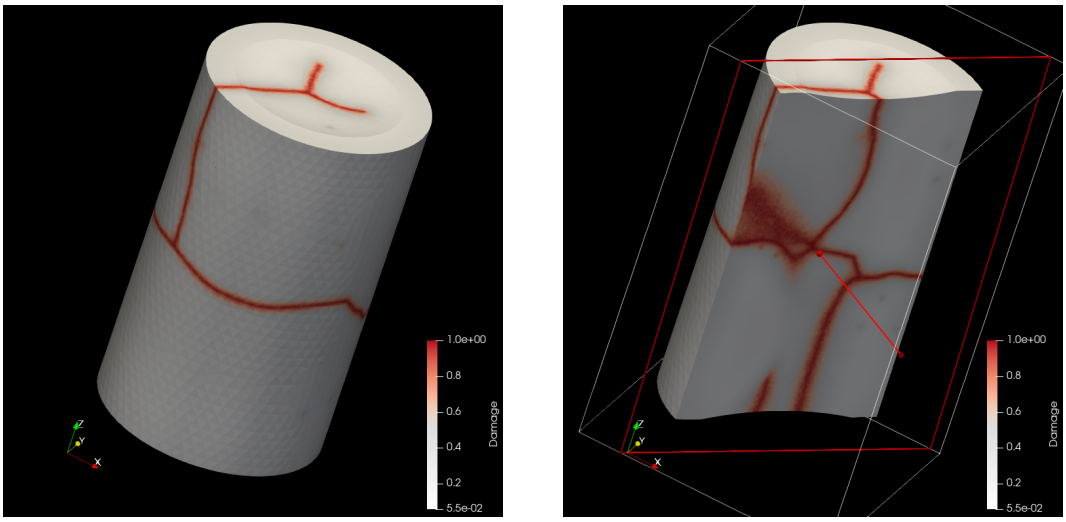

Figure 12. Crack pattern

6. Conclusions and perspectives

This work has investigated the use of micromorphic behaviours for the description of quasi-brittle materials and has shown that those micromorphic behaviours can be considered as varitionaly consistent approximations of standard phase-field models. Three alternate minimization schemes, which are straightforward to implement in standard FEM or FFT solvers, have been proposed, and their numerical performance has been investigated intensively using representative tests. Convergence of those schemes is guaranteed but requires a large number of fixed-point iterations. Regarding this observation, the third scheme appears to be more efficient.

The proposed approach can be extended to more complex damage behaviours and ductile failure. Finally, as a future work, acceleration schemes could also be investigated to reduce the number of fixed-point iterations.

Aknowledgements

The work presented in this paper was conducted in the framework of the PLEIADES project, which was supported financially by the CEA (Commissariat à l'Énergie Atomique et aux Énergies Alternatives), EDF (Électricité de France) and Framatome.

References

[1] G. Francfort, J.-J. Marigo, Revisiting brittle fracture as an energy minimization problem, Journal of the Mechanics and Physics of Solids 46 (8) (1998) 1319–1342. doi:10.1016/S0022-5096(98)00034-9.
URL https://linkinghub.elsevier.com/retrieve/pii/S0022509698000349

[2] G. Francfort, J.-J. Marigo, Vers une théorie énergétique de la rupture fragile, Comptes Rendus Mécanique 330 (4) (2002) 225–233. doi:10.1016/S1631-0721(02)01454-7.
URL https://linkinghub.elsevier.com/retrieve/pii/S1631072102014547

[3] B. Bourdin, G. Francfort, J.-J. Marigo, Numerical experiments in revisited brittle fracture, Journal of the Mechanics and Physics of Solids 48 (4) (2000) 797–826. doi:10.1016/S0022-5096(99)00028-9.
URL https://linkinghub.elsevier.com/retrieve/pii/S0022509699000289

[4] A. Chambolle, S. Conti, G. A. Francfort, Approximation of a Brittle Fracture Energy with a Constraint of Non-interpenetration, Archive for Rational Mechanics and Analysis 228 (3) (2018) 867–889. doi:10.1007/s00205-017-1207-z.
URL https://doi.org/10.1007/s00205-017-1207-z

[5] L. Ambrosio, V. M. Tortorelli, Approximation of functional depending on jumps by elliptic functional via t-convergence, Communications on Pure and Applied Mathematics 43 (8) (1990) 999–1036.

[6] T. Gerasimov, L. De Lorenzis, Numerical Implementation of Phase-Field Models of Brittle Fracture, in: Modeling in Engineering Using Innovative Numerical Methods for Solids and Fluids, CISM International Centre for Mechanical Sciences, Springer International Publishing, 2020.
URL https://www.springerprofessional.de/en/numerical-implementation-of-phase-field-models-of-brittle-fractu/17664414

[7] B. Bourdin, J.-J. Marigo, C. Maurini, P. Sicsic, Morphogenesis and propagation of complex cracks induced by thermal shocks, Physical Review Letters 112 (2014) 014301. doi:10.1103/PhysRevLett.112.014301.
URL https://link.aps.org/doi/10.1103/PhysRevLett.112.014301

[8] L. D. Lorenzis, E. Zurich, T. Gerasimov, Numerical implementation of phase-field models of brittle fracture euclid-efficient unsupervised constitutive law identification and discovery view project crack phase-field computation in multiphase porous materials view projectdoi:10.1007/978-3-030-37518-8_3.
URL https://doi.org/10.1007/978-3-030-37518-8_3

[9] G. D. Piero, G. Lancioni, R. March, A variational model for fracture mechanics: Numerical experiments, Journal of the Mechanics and Physics of Solids 55 (2007) 2513–2537. doi:10.1016/J.JMPS.2007.04.011.

[10] A. Chambolle, S. Conti, G. A. Francfort, Approximation of a brittle fracture energy with a constraint of non-interpenetration, Arch. Rational Mech. Anal 228 (2018) 867–889. doi:10.1007/s00205-017-1207-z.
URL https://doi.org/10.1007/s00205-017-1207-z

[11] T. Gerasimov, L. D. Lorenzis, On penalization in variational phase-field models of brittle fracture, Computer Methods in Applied Mechanics and Engineering 354 (2019) 990–1026. doi:10.1016/J.CMA.2019.05.038.

[12] B. Bourdin, G. A. Francfort, J.-J. Marigo, The variational approach to fracture 91 (2008) 5–148. doi:10.1007/s10659-007-9107-3.

[13] C. Miehe, M. Hofacker, F. Welschinger, A phase field model for rate-independent crack propagation: Robust algorithmic implementation based on operator splits, Computer Methods in Applied Mechanics and Engineering 199 (45-48) (2010) 2765–2778. doi:10.1016/j.cma.2010.04.011.
URL https://linkinghub.elsevier.com/retrieve/pii/S0045782510001283

[14] S. Forest, Micromorphic Approach for Gradient Elasticity, Viscoplasticity, and Damage, Journal of Engineering Mechanics 135 (3) (2009) 117–131. doi:10.1061/(ASCE)0733-9399(2009)135:3(117).
URL http://ascelibrary.org/doi/10.1061/%28ASCE%290733-9399%282009%29135%3A3%28117%29

[15] S. Forest, Nonlinear regularization operators as derived from the micromorphic approach to gradient elasticity, viscoplasticity and damage, Proceedings of the Royal Society A: Mathematical, Physical and Engineering Sciences 472 (2188) (2016) 20150755. doi:10.1098/rspa.2015.0755.
URL https://royalsocietypublishing.org/doi/abs/10.1098/rspa.2015.0755

[16] M. Rezaee-Hajidehi, S. Stupkiewicz, Micromorphic approach to phase-field modeling of multivariant martensitic transformation with rate-independent dissipation effects, International Journal of Solids and Structures 222-223 (2021) 111027. doi:10.1016/j.ijsolstr.2021.03.014.
URL https://www.sciencedirect.com/science/article/pii/S0020768321001050

[17] R. Bharali, Computational homogenisation and solution strategies for phase-field fracture, phdthesis, Chalmers university of technology, Gothenburg, Sweden (2021).

[18] J. J. Moreau, Sur les lois de frottement, de plasticité et de viscosité, Compte Rendu de l'Académie des Sciences série A 271 (1970) 608–611.

[19] B. Halphen, Q. S. Nguyen, Sur les matériaux standard généralisés, Journal de Mécanique 14 (1) (1975) 39–63.

[20] A. Ehrlacher, Principe d'extremum et équation en vitesse pour les systèmes à dissipation simple, in: 7ème Congrès Français de Mécanique, Actes du CFM 1985, 1985, event-place: Bordeaux, France.

[21] Q.-S. Nguyen, Standard dissipative systems and stability analysis, in: G. A. Maugin, R. Drouot, F. Sidoroff (Eds.), Continuum Thermomechanics: The Art and Science of Modelling Material Behaviour, Solid Mechanics and Its Applications, Springer Netherlands, Dordrecht, 2002, pp. 343–354. doi:10.1007/0-306-46946-4_26.
URL https://doi.org/10.1007/0-306-46946-4_26

[22] E. Lorentz, S. Andrieux, A variational formulation for nonlocal damage models, International Journal of Plasticity 15 (2) (1999) 119–138. doi:10.1016/S0749-6419(98)00057-6.
URL https://linkinghub.elsevier.com/retrieve/pii/S0749641998000576

[23] S. Forest, E. Lorentz, Localization phenomena and regularization methods, in: J. Besson (Ed.), Local approach to fracture, Ecole d'été "Mécanique de l'endommagement et approche locale de la rupture" (MEALOR), juillet 2004, Les presses de l'ecole des mines de paris, 2004, pp. 311–371.
URL https://hal.archives-ouvertes.fr/hal-00164479

[24] N. Q. Son, On standard gradient plasticity and visco-plasticity, International Journal of Solids and Structures 225 (2021) 111038. doi:10.1016/j.ijsolstr.2021.111038.
URL https://www.sciencedirect.com/science/article/pii/S0020768321001220

[25] R. Alessi, J.-J. Marigo, S. Vidoli, Gradient damage models coupled with plasticity: Variational formulation and main properties, Mechanics of Materials 80 (2015) 351–367. doi:10.1016/j.mechmat.2013.12.005.
URL https://linkinghub.elsevier.com/retrieve/pii/S0167663614000039

[26] B. Bourdin, A. Chambolle, Implementation of an adaptive finite-element approximation of the Mumford-Shah functional:, Numerische Mathematik 85 (4) (2000) 609–646. doi:10.1007/PL00005394.
URL http://link.springer.com/10.1007/PL00005394

[27] K. Pham, J. Marigo, Approche variationnelle de l'endommagement : I. Les concepts fondamentaux, Comptes Rendus Mécanique 338 (2010) 191–198.

[28] K. Pham, Construction et analyse de modèles d'endommagement à gradient, Ph.D. thesis (2010).

[29] E. Lorentz, V. Godard, Gradient damage models: Toward full-scale computations, Computer Methods in Applied Mechanics and Engineering

200 (21-22) (2011) 1927–1944. doi:10.1016/j.cma.2010.06.025.
URL https://linkinghub.elsevier.com/retrieve/pii/S0045782510001921

[30] E. Lorentz, S. Cuvilliez, K. Kazymyrenko, Convergence of a gradient damage model toward a cohesive zone model, Comptes Rendus Mécanique 339 (1) (2011) 20–26. doi:10.1016/j.crme.2010.10.010.
URL http://www.sciencedirect.com/science/article/pii/S1631072110001671

[31] E. Azinpour, J. P. S. Ferreira, M. P. L. Parente, J. C. de Sa, A simple and unified implementation of phase field and gradient damage models, Advanced Modeling and Simulation in Engineering Sciences 5 (1) (2018) 15. doi:10.1186/s40323-018-0106-7.
URL https://doi.org/10.1186/s40323-018-0106-7

[32] R. Alessi, F. Freddi, L. Mingazzi, Phase-field numerical strategies for deviatoric driven fractures, Computer Methods in Applied Mechanics and Engineering 359 (2020) 112651. doi:10.1016/j.cma.2019.112651.
URL https://linkinghub.elsevier.com/retrieve/pii/S0045782519305365